Review of Scientific Instruments

Post-acquisition mask misalignment correction for edge illumination x-ray phase contrast imaging

Cite as: Rev. Sci. Instrum. **93**, 053706 (2022); https://doi.org/10.1063/5.0090517
Submitted: 07 March 2022 • Accepted: 05 May 2022 • Published Online: 24 May 2022
Published open access through an agreement with JISC Collections

D. Shoukroun, A. Doherty, M. Endrizzi, et al.

Review of Scientific Instruments ARTICLE scitation.org/journal/rsi

Post-acquisition mask misalignment correction for edge illumination x-ray phase contrast imaging

Cite as: Rev. Sci. Instrum. 93, 053706 (2022); doi: 10.1063/5.0090517
Submitted: 7 March 2022 • Accepted: 5 May 2022 •
Published Online: 24 May 2022

D. Shoukroun,[1,a)] A. Doherty,[1] M. Endrizzi,[1] D. Bate,[2] P. Fromme,[3] and A. Olivo[1]

AFFILIATIONS

[1] Department of Medical Physics and Biomedical Engineering, University College London, London WC1E 6BT, United Kingdom
[2] Nikon, X-Tek Systems, Ltd., Tring, Hertfordshire HP23 4JX, United Kingdom
[3] Department of Mechanical Engineering, University College London, London WC1E 6BT, United Kingdom

[a)] **Author to whom correspondence should be addressed:** dana.shoukroun.17@ucl.ac.uk

ABSTRACT

Edge illumination x-ray phase contrast imaging uses a set of apertured masks to translate phase effects into variation of detected intensity. While the system is relatively robust against misalignment, mask movement during acquisition can lead to gradient artifacts. A method has been developed to correct the images by quantifying the misalignment post-acquisition and implementing correction maps to remove the gradient artifact. Images of a woven carbon fiber composite plate containing porosity were used as examples to demonstrate the image correction process. The gradient formed during image acquisition was removed without affecting the image quality, and results were subsequently used for quantification of porosity, indicating that the gradient correction did not affect the quantitative content of the images.

INTRODUCTION

X-ray Phase Contrast Imaging (XPCi) offers an alternative when conventional attenuation-based x-ray imaging suffers from poor contrast.[1] XPCi arises from the real part (δ) of the refractive index n, as opposed to the imaginary part (β) used in conventional attenuation-based x-ray imaging. Changes in phase are always present in x-ray imaging, but are not detected by conventional setups.[2,3] Different experimental setups were developed to convert changes in phase into changes in intensity, which can be measured with standard x-ray detectors, such as Talbot-Lau (grating) interferometry,[4] free space propagation,[5] and analyzer-based XPCi.[6] Edge Illumination (EI) XPCi is a differential phase technique (i.e., sensitive to the first derivative of the phase) that relies on the x-ray beam only illuminating the edge of the pixel's active surface.[7] It uses two apertured masks to split the beam into multiple beamlets and analyzes the beamlets' dampening, deviation, and broadening. This allows the retrieval of three contrast channels: conventional attenuation, differential phase (or refraction) signal, and dark-field, the latter corresponding to ultra-small-angle scattering due to sub-pixel features.[8] EI XPCi works effectively at relatively high x-ray energy and divergent and polychromatic beams, and it can achieve an angular resolution down to hundreds of nanoradians in standard laboratory environments.[9]

Problems that can be encountered during the acquisition of an EI XPCi sequence include misalignment of the apertured masks. The robustness against potential misalignment has been previously tested;[10] however, larger displacements can lead to gradients across the differential phase images. Artifacts occurring due to components' movement during acquisition were previously observed in other XPCi methods, notably in grating-based XPCi, where a variation in phase stepping (i.e., relative movement of one of the gratings) leads to fringe artifacts in the retrieved images.[11,12] Here, a post-acquisition correction tool for the removal of artifacts caused by the movement of the apertured masks during the image acquisition, or by their initial misalignment, is proposed. The pre-acquisition mask alignment procedure is explained, and the post-processing method derived directly from it is described. The post-acquisition correction process was implemented on images of carbon-fiber reinforced plastic (CFRP)

plates containing porosity, used previously for planar XPCi porosity quantification.[13]

EXPERIMENTAL SETUP

An EI XPCi system, including a Rigaku MicroMax 007 HF rotating anode 40 kVp molybdenum source, operated at 20 mA with a 70 μm focal spot was used; a schematic of the system is shown in Fig. 1. The detector used was a Hamamatsu C9732DK flat panel CMOS detector with a pixel size of 50 × 50 μm^2. The source-to-detector distance was 0.85 m, and the source-to-sample distance was 0.6 m. A pair of apertured masks was provided by Creatv Microtech (Potomac, MD), consisting of an ~120 μm thick gold layer electroplated on a patterned graphite substrate. The first ("sample") mask was placed 0.05 m upstream of the sample stage. It had an aperture width of 10 μm and a period of 79 μm. The second ("detector") mask was placed immediately before the detector and had an aperture of 17 μm and a period of 98 μm.

The imaged sample was part of a series of cross-ply woven carbon fiber reinforced composite plates, 3 mm in thickness, containing variable amounts of porosity (results shown for a sample with 3.4% porosity). The aim was to quantify the variation in porosity through the phase-based signals using planar XPCi instead of the conventional x-ray CT imaging used for porosity quantification, meaning that conserving the quantitative signal post-correction was a priority.[13] However, the correction procedure is independent of the imaged sample, which is segmented out so that only background regions are used to correct the gradients (see below).

The acquisition process included the acquisition of 19 exposures without a sample in the beam, corresponding to 19 points on the illumination curve (IC), with nine points taken symmetrically on either side of the curve, plus one at the top corresponding to the position where the two masks are perfectly aligned. The IC is a bell-shaped curve representing the variation of the detected intensity for different sample mask positions relative to the (stationary and aligned) detector mask/detector combination, which can be approximated by a Gaussian.[14]

The sample mask was displaced in 2 μm steps along the x-direction between each IC point. Corresponding images with the sample present were then acquired at the same mask positions. To increase the image statistics and resolution, the exposure time per mask position was set to 6 s. As part of the sample is obscured by the mask septa, the above procedure was repeated while the sample was moved along the x-axis in subpixel steps to ensure full sample illumination. Those images are then interwoven together post-acquisition—a process known as dithering. Here, 16 dithering steps were used to maximize resolution and statistics, allowing for a

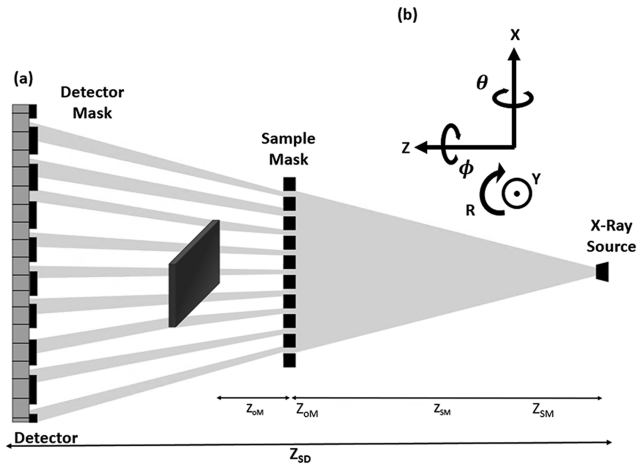

FIG. 1. EI XPCi experimental setup (a) with respective transitional and rotational degrees of freedom of the EI XPCI system (b), θ rotation around the x-axis, R rotation around the y-axis, and ϕ rotation around the z-axis.

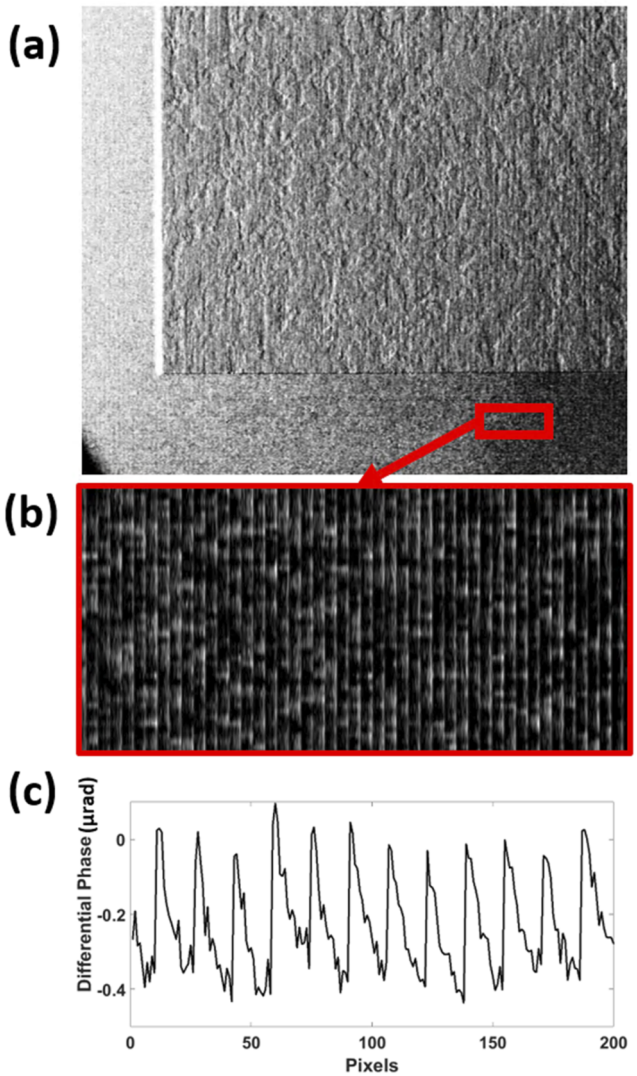

FIG. 2. Dithering artifact (b) observed in the retrieved differential phase image of the composite plate sample (a). Periodic variation of the retrieved refraction angle (in μrad) is observed (c) following recombination of the 16 dithering steps.

better assessment of the efficacy of the correction procedure. The retrieval of the attenuation, differential phase, and dark-field signals was achieved by fitting a Gaussian to the intensity measured for all sample mask positions, for sequences acquired both with and without the sample. Comparing the parameters of the two Gaussians allows extracting the different contrast channels.[15] The attenuation signal corresponds to the reduction in the area under the Gaussian, the differential phase signal corresponds to the shift in its central position, and the dark-field signal corresponds to its relative broadening.

Figure 2 shows the resulting gradient across the differential phase image of a composite plate (3.4% porosity) due to displacement of the masks. In this case, as the overall homogeneity of the sample was investigated to quantify porosity artifacts, the misalignment-induced gradients affected the image uniformity, thus interfering with the porosity-induced signal. This gradient, with the image background becoming increasingly darker toward the bottom right corner, occurred due to the particularly long scan times needed for these specimens (hour vs minutes for a standard planar image). Additional to the image-wide gradient, a variation was observed across the dithering steps (i.e., every 16 pixels), resulting from some steps having higher baseline signals compared to others, leading to a variation in intensity. The relative movement of the masks can be tracked between dithering steps, with the average background signal decreasing across each pixel in the 16-pixel period. The presence of this second artifact indicates that the dithering step images need to be corrected on an individual basis, as opposed to applying a single correction to the entire post-recombination, higher resolution image.

METHODOLOGY

An investigation about the optimal mask alignment technique was previously presented,[16] where the alignment of the masks was split into six degrees of freedom (Fig. 1). Three translational degrees of freedom (x, y, and z) and three rotational degrees of freedom (θ, R, and ϕ) must be accounted for, representing the rotation around the three main translational directions. The misalignment of the masks can be represented through a 2D function, denoted G, which is a smooth, continuous surface representing the central position of the IC on a pixel-by-pixel basis. The authors of Ref. 16 showed that the misalignments along each degree of freedom can be translated into a specific and independent feature (i.e., gradient) in the shape of G. These features are expressed as a function of the position of each pixel in the detector, and the four significant features are shown in Fig. 3. For example, the feature associated with misalignment along the z-axis is defined as S_z and appears as a horizontal gradient in G. Using these features, the overall masks' misalignment function G can be expressed as

$$G = a_0 + a_z S_Z + a_\phi S_\phi + a_\theta S_\theta + a_R S_R + \varepsilon, \quad (1)$$

where a_0 represents a baseline value (corresponding to the alignment along the x-axis); S_Z, S_ϕ, S_θ, and S_R are the surfaces representing misalignments along their respective degrees of freedom; a_z, a_ϕ, a_θ, and a_R are their respective weighting coefficients; and ε represents the combination of random and systematic noise. The alignment along the y-axis is neglected for the system used here, as the apertures in the sample and detector masks consist of long parallel slits in the y direction, making the alignment along the y-axis irrelevant.

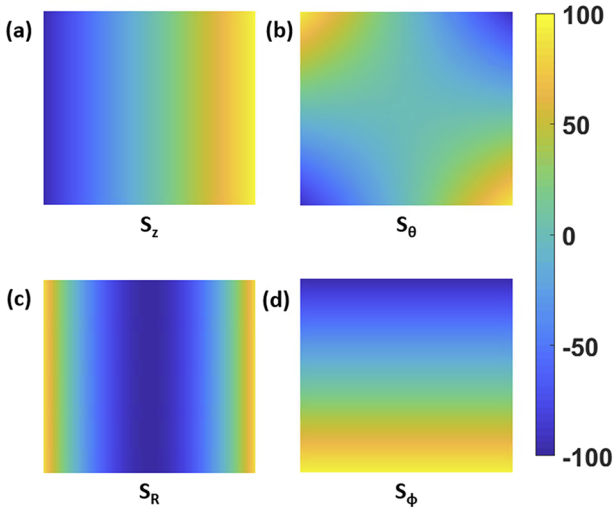

FIG. 3. Features of G can be directly associated with misalignments along the separate degrees of freedom of mask movement. (a) S_z, (b) S_θ, (c) S_R, and (d) S_φ. The surface G can be decomposed into a superposition of these features. Color bar showing variation in detected intensity as a percentage due to mask misalignments.

To obtain alignment, prior to image acquisition an IC is acquired, the optimal sample mask position relative to the detector mask is calculated, and a series of motors are moved accordingly to place the sample mask in the calculated (aligned) position. However, as discussed, the mask(s) can move during acquisition, especially if this is particularly long. The developed method creates a correction map that calculates the effect of the misalignment along the different degrees of freedom using the background area of the images and subtracts it from the retrieved sample images. As the surface G is usually fitted to a retrieved differential phase image without any sample in place, fitting G to the sample free area allows calculating the mask movement that has occurred since the initial mask alignment. Instead of using the information from this fit to realign the masks, we propose a solution where the flat field distortions caused by this misalignment (i.e., the curves in 2D described by the function G) are removed from the differential phase images.

IMPLEMENTATION AND DISCUSSION

Since a different gradient was observed across the individual dithering steps (causing the dithering artifact observed in Fig. 2), the movement of the masks was tracked using the images acquired at each individual dithering step. In each image, the average signal in different sample-free areas was used to estimate the relative mask movement and correct for it. As can be observed from Fig. 4, a clear variation in background intensity could be observed. A first gradient in the x-direction can be observed in Figs. 4(b) and 4(c), indicating a slight translation of the mask along the z-axis, an effect known from previous observations,[16] and shown in Fig. 3(a). Similarly, a second gradient can be observed in the y-direction by noting that

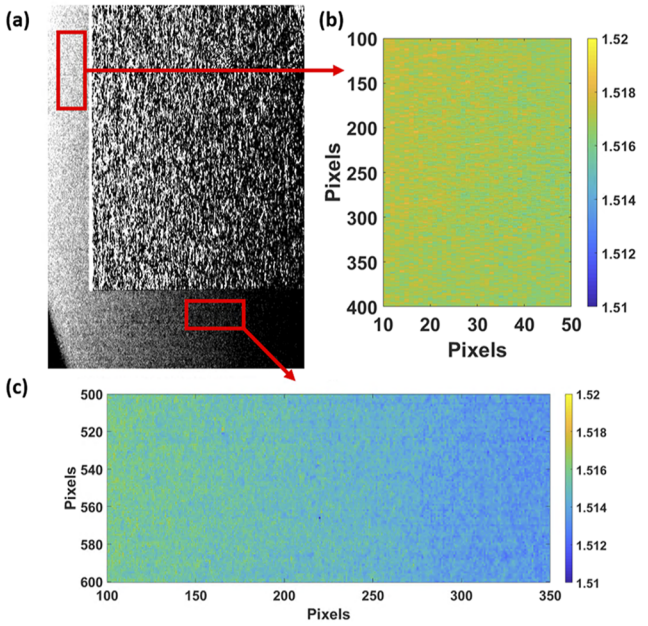

FIG. 4. Variation in intensity (in μrad) observed across a single dithering step of the differential phase image (a), both in the top left corner (b) and the bottom right corner (c), indicated by red rectangles in (a), showing the gradient across the image, used to estimate the type of misalignments involved in each dithering step.

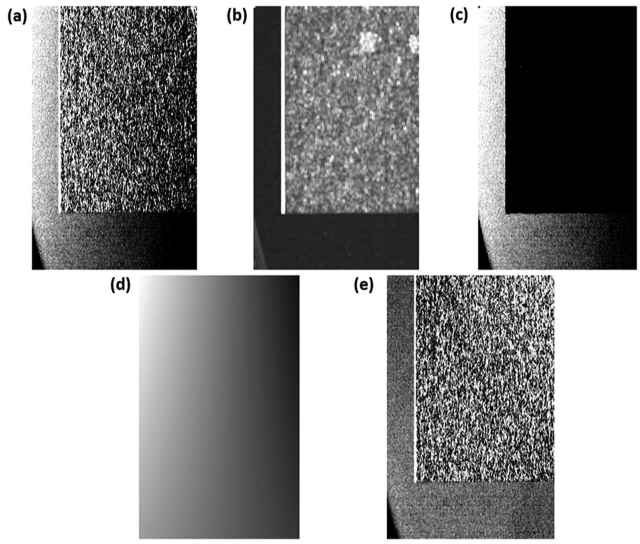

FIG. 5. Image of the refraction signal (a) and the standard deviation of the differential phase (b) obtained from a single dithering step image, calculated on a pixel-by-pixel basis over an area of 7 × 7 pixels^2, used to segment the sample using the thresholding method (c); correction map (d) created by fitting Eq. (1) to the background and corrected image (e) obtained from subtracting the correction map from the initial dithering step image.

the average intensity in Figs. 4(b) and 4(c) shows a clear decrease, indicating a rotation of the mask around the z-axis [similar to the gradient observed in Fig. 3(d)].[16]

To remove this gradient, a correction map was created by fitting a polynomial, P(x,y), that reproduces Eq. (1) to the background area signal at each individual dithering step such that

$$P(x,y) = ax^2 + bxy + cx + dy + n, \tag{2}$$

where each parameter describes the surface misalignments along different degrees of freedom. As such, x^2 represents the surface misalignment S_R, xy represents S_θ, x represents S_Z, and y represents S_φ. $a, b, c,$ and d are their respective weighting coefficients, and n is an offset parameter accounting for random and systematic noise.

These background areas were obtained by segmenting out the sample using a thresholding technique based on the standard deviation of the differential phase image, calculated over a rolling 7 × 7 pixel^2 window [see Fig. 5(b)]. This was based on the observation that the standard deviation of the background was substantially lower than that of the sample. The resulting thresholded image is shown in Fig. 5(c), which allows for an easier segmentation of the sample and background areas. The sample was segmented and only the background area of the image was used to ensure that the signal from the sample does not influence the calculated misalignment surfaces and to create a generalized approach that is not sample-dependent.

A correction map was created by fitting Eq. (1) onto the (thresholded) background area, with the result of the fit shown in Fig. 5(d). It should be noted that the correction is only possible if some background area (empty space) is available in the image and cannot be applied if the sample occupies the entire field of view. The process was repeated for all dithering steps, and all correction maps were then subtracted from their corresponding images; Fig. 5(e) shows the corrected image for that specific dithering step. The dithering steps were then recombined to form the higher

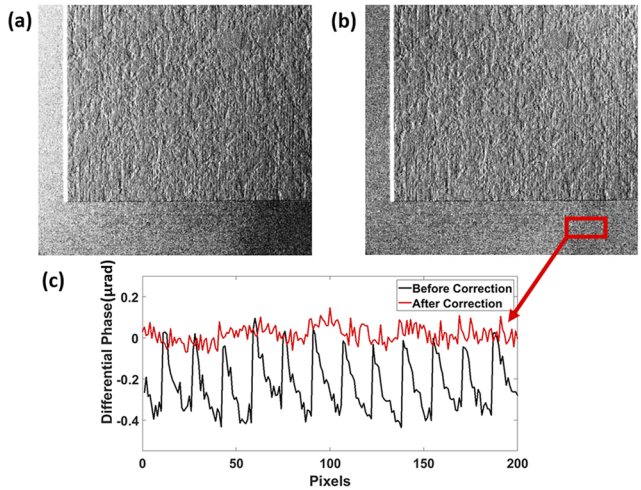

FIG. 6. Refraction image including recombination of all dithering steps before [(a); black] and after [(b); red] the gradient correction; corresponding profiles of background area (c).

resolution differential phase image: a comparison between recombined images before and after the correction process is shown in Fig. 6.

The contrast was stretched to enhance the change in the background from one image to another. A clear improvement can be observed after implementation of the gradient correction: in quantitative terms, the background of the corrected image is uniform and has an average background signal close to zero (5 ± 8 nrad), while this is 0.2 ± 0.2 μrad in the uncorrected image [Fig. 6(c)], i.e., a 40-fold improvement in the background signal. Moreover, the dithering artifact observed in Fig. 2(c) is no longer present due to the correction being applied at each individual dithering step, i.e., each dithering step (effectively an independent measurement of the same quantity) is reported to the same baseline.

Images corrected using this approach were used to show that the standard deviation of the differential phase signal can be used to quantify porosity in the set of carbon fiber reinforced composites used in this investigation by comparing it to ultrasonic signal attenuation.[13] A clear correlation between the standard deviation of the differential phase signal and the ultrasonic attenuation signal was observed for varying degrees of porosity, demonstrating the reliability of the post-correction differential phase signal.

CONCLUSIONS

While EI XPCi is reasonably robust against vibrations and other complications associated with a standard laboratory environment, it can still be subject to mask misalignment, especially if these drift during long acquisitions in environments with non-negligible levels of vibrations. When this happens, gradients across the images and dithering artifacts can be observed. A post-processing method was presented, which allows us to correct for such artifacts in the differential phase channel by creating correction maps of the evaluated misalignments that are then subtracted from the images. This requires a background area in the image, meaning that this is not possible for samples that occupy the entire field of view. The correction allows removing the gradient artifacts from the images without affecting the imaged sample.

ACKNOWLEDGMENTS

This work was supported by the UK Engineering and Physical Sciences Research Council (EPSRC) (Grant Nos. EP/N509577/1, EP/T005408/1, and EP/R513143/1). A.O. was supported by the Royal Academy of Engineering under the Chairs in Emerging Technologies scheme.

AUTHOR DECLARATIONS

Conflict of Interest

The authors have no conflicts to disclose.

Author Contributions

D.S. and A.D. contributed equally to this work.

DATA AVAILABILITY

The data that support the findings of this study are available from the corresponding author upon reasonable request.

REFERENCES

[1] A. Momose, Jpn. J. Appl. Phys. **44**, 6355 (2005).
[2] V. Revol, C. Kottler, R. Kaufmann, U. Straumann, and C. Urban, Rev. Sci. Instrum. **81**, 073709 (2010).
[3] A. Bravin, P. Coan, and P. Suortti, Phys. Med. Biol. **58**, R1 (2013).
[4] C. Gusenbauer, M. Reiter, B. Plank, D. Salaberger, S. Senck, and J. Kastner, J. Nondestruct. Eval. **38**, 1 (2019).
[5] P. Cloetens, M. Pateyron-Salomé, J. Y. Buffière, G. Peix, J. Baruchel, F. Peyrin, and M. Schlenker, J. Appl. Phys. **81**, 5878 (1997).
[6] A. Bravin, J. Phys. D. Appl. Phys. **36**, A24 (2003).
[7] A. Olivo and R. Speller, Phys. Med. Biol. **52**, 6555 (2007).
[8] M. Endrizzi, P. C. Diemoz, C. K. Hagen, T. P. Millard, F. A. Vittoria, U. H. Wagner, C. Rau, I. K. Robinson, and A. Olivo, in *2014 IEEE Nuclear Science Symposium and Medical Imaging Conference NSS/MIC 2014* (IEEE, 2016), Vol. 1.
[9] A. Astolfo, M. Endrizzi, G. Kallon, T. P. Millard, F. A. Vittoria, and A. Olivo, J. Phys. D. Appl. Phys. **49**, 485501 (2016).
[10] M. Endrizzi, D. Basta, and A. Olivo, Appl. Phys. Lett. **107**, 124103 (2015).
[11] F. De Marco, M. Marschner, L. Birnbacher, P. Noël, J. Herzen, and F. Pfeiffer, Opt. Express **26**, 12707 (2018).
[12] J. Chen, J. Zhu, Z. Li, W. Shi, Q. Zhang, Z. Hu, H. Zheng, D. Liang, and Y. Ge, Phys. Med. Biol. **64**, 195013 (2019).
[13] D. Shoukroun, L. Massimi, M. Endrizzi, D. Bate, P. Fromme, and A. Olivo, Proc. SPIE **11593**, 115932 (2021).
[14] M. Endrizzi, P. C. Diemoz, T. P. Millard, J. Louise Jones, R. D. Speller, I. K. Robinson, and A. Olivo, Appl. Phys. Lett. **104**, 024106 (2014).
[15] N. Matsunaga, K. Yano, M. Endrizzi, and A. Olivo, J. Phys. D. Appl. Phys. **53**, 095401 (2020).
[16] A. Doherty, L. Massimi, A. Olivo, and M. Endrizzi, Nucl. Instrum. Methods Phys. Res., Sect. A **984**, 164602 (2020).